

Interplay between resource dynamics, network structure and spatial propagation of transient explosive synchronization in an adaptively coupled mouse brain network model

Avinash Ranjan¹, Saurabh R. Gandhi^{*1}

¹Department of Electrical Engineering, Indian Institute of Technology Delhi, New Delhi, India

Corresponding author: Saurabh R. Gandhi, e-mail: gsaurabhr@iitd.ac.in

Abstract

Generalized epileptic attacks, which exhibit widespread disruption of brain activity, are characterized by recurrent, spontaneous and synchronized bursts of neural activity that self-initiate and self-terminate through critical transitions. Here we utilize the general framework of explosive synchronization (ES) from complex systems science to study the role of network structure and resource dynamics in the generation and propagation of seizures. We show that a combination of resource constraint and adaptive coupling in a Kuramoto network oscillator model can reliably generate seizure-like synchronization activity across different network topologies, including a biologically derived mesoscale mouse brain network. The model, coupled with a novel algorithm for tracking seizure propagation, provides mechanistic insight into the dynamics of transition to the synchronized state and its dependence on resources; and identifies key brain areas that may be involved in the initiation and spatial propagation of the seizure. The model, though minimal, efficiently recapitulates several experimental and theoretical predictions from more complex models, and makes novel experimentally testable predictions.

Significance statement / Author Summary

Understanding seizure dynamics at the whole-brain level is crucial for controlling abnormal hypersynchronous activity. Currently, complete brain coverage recordings are lacking in both patients and animal models. We employ network science tools to investigate epileptic seizure-like synchronization in a mouse whole brain network, leveraging network structure and supported dynamics as the basis for seizure evolution. Our results align with experimental findings, suggesting that seizure activity initiates in the cortico-thalamic circuit. Importantly, our novel analysis identifies key nodes, primarily in the cortex, driving this hypersynchronous activity. Our findings highlight network structure's role in shaping seizure dynamics and the techniques developed here could enhance our control of generalized seizures when combined with patient-specific data.

Keywords

epilepsy, mouse brain connectome, explosive synchronization, adaptive coupling, seizure propagation, resource dynamics

34 Introduction

35 Epileptic seizures, characterized by bursts of excessive neuronal synchronization which usually self-initiate and
 36 self-terminate, are considered as a dynamical disease of brain networks ¹. Seizures can be classified into
 37 distinct subtypes, broadly including those that are confined to a circumscribed area (focal) and those which
 38 involve larger sections of the brain (generalized) ². A wide range of microscopic mechanisms contribute to this
 39 limited repertoire of seizure types ³. Although seizures can originate from different brain regions in patients,
 40 they may still manifest similar macroscopic features, as seen in EEG recordings³⁻⁵. Furthermore, studies have
 41 suggested that seizures with similar microscopic mechanisms can present as either focal or generalized
 42 depending on the macroscopic network structure ⁶. This decoupling between microscopic and macroscopic
 43 dynamics underscores the importance of directly modeling emergent properties of seizures and highlights the
 44 significance of adopting a network level approach to studying epilepsy, which has also been recognized by the
 45 International League Against Epilepsy ⁷.

46 Experimental evidence shows that network structure alone is not sufficient but the dynamics supported by it
 47 also plays an important role in seizure generation and propagation in a brain network ^{8,9}. Seizures have been
 48 hypothesized to exist in the bistable regime of dynamical networks that exhibits multiple stable states – normal
 49 (unsynchronized) and abnormal (hyper-synchronized). In such a system, random fluctuations (noise) or
 50 resource availability can transition the network between the different states, giving rise to transient
 51 hyper-synchronized activity seen during epileptic seizures ^{1,10}.

52 The phenomenon of explosive synchronization (**ES**) that is widely studied in complex systems and network
 53 science can provide a general framework to understand the role of network structure in facilitating seizure
 54 dynamics ¹¹⁻¹⁴. ES is characterized by first order, discontinuous and irreversible transitions between globally
 55 coherent and incoherent states. These features are highly relevant to seizure dynamics, which also show
 56 signatures of critical transitions at both onset and termination across multiple spatial scales ^{15,16}. Consequently,
 57 ES models have been employed to study abrupt transitions in brain networks ^{17,18}. Moreover, complete brain
 58 coverage recordings, which can elucidate the dynamics of generalized seizures, are lacking in both patient and
 59 animal models. Thus, integrating ES with biological networks enables the study of seizure-like synchronization
 60 dynamics at the whole-brain level.

61 Although ES in complex networks has been successfully modeled using two common microscopic
 62 mechanisms – the presence of microscopic correlation features, such as frequency-degree coupling (**FDC**);
 63 and adaptive coupling ^{12,14} – they do not explain the transient and recurrent nature of seizures. Experimental
 64 and computational studies have linked this transient nature of seizures with the dynamics of energy
 65 metabolism ^{4,10}. Consistent with this observation, a recent study has shown the occurrence of transient ES
 66 (**tES**) in a resource-constrained scale-free network with FDC ¹⁹, where the time-varying nature of resource
 67 consumption is shown to cause the transient behavior.

68 While resource constrained networks with FDC exhibit tES for certain scale-free networks, there are several
 69 other frequently occurring families of network structures (Fig. 1a-c) across which this mechanism does not
 70 appear to generalize. Especially in the context of neural dynamics, the network structure of brains (Fig. 1d) is
 71 often found to show characteristics of small-world networks (SWNs) as well as scale-free networks (SFNs)
 72 (Fig. 1e,f). Moreover, adaptive coupling schemes have been shown to exhibit ES more generally across
 73 several network topologies, and in fact ES has been suggested to be a generic property of networks with
 74 adaptive coupling ¹⁴. Adaptive coupling is biologically plausible and has often been used to model interaction in
 75 biological systems ²⁰. Therefore in this study, we combine resource-constraint with adaptive coupling in a
 76 model (Fig. 1g) that can manifest tES across several types of network structures, including classic small-world

77 and scale-free networks as well as a real biological network (a mesoscale mouse brain network, MBN,
78 obtained from the Allen Institute public dataset²¹).

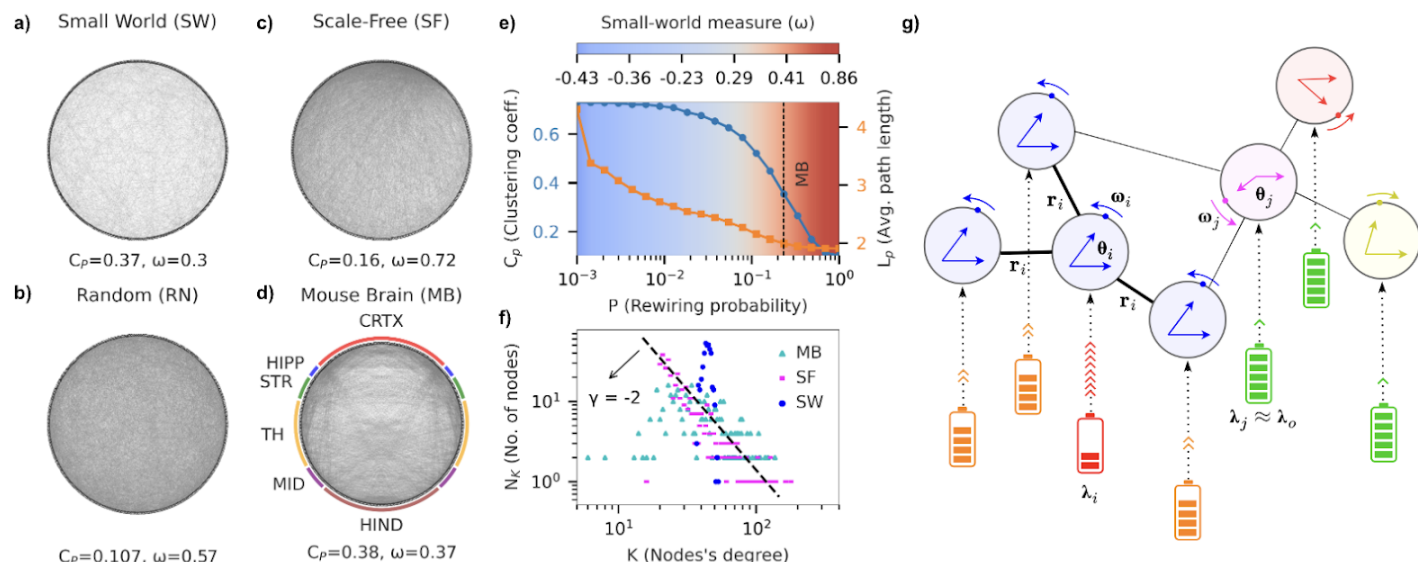


Figure 1: A model with adaptive coupling and resource constraint manifests transient explosive synchronization (tES) in the mesoscale mouse brain network (MBN), that shows both scale-free (SFN) and small-world (SWN) properties

a) Visualization of a small-world (SW) network generated using the Watts-Strogatz algorithm (number of nodes, $N=400$, average degree, $\langle k \rangle=40$, rewiring probability, $p=0.232$). The generated network has average path length ($L_p=1.97$) and clustering coefficient ($C_p=0.37$) similar to mouse brain (MB) network; and small-world measure, $\omega=0.3$. **b)** Random network with path length and average degree matched to MB ($L_p=1.89$, $\langle k \rangle=45$). **c)** Whole mouse brain mesoscale network having 426 nodes (213 in each hemisphere), each representing a region in mesoscale connectome from Allen mouse brain atlas. The color coded ring around the MB network groups the 426 nodes into 6 major regions (Cortex (CRTX), Hippocampus (HIPP), Striatum (STR), Thalamus and Hypothalamus (TH), Midbrain (MID), Hindbrain (HIND)). The graph ($L_p=2.1$, $\omega=0.37$) is generated using a binarized version of the weighted network to allow for comparison with SW and scale-free (SF) networks. **d)** Scale-free ($L_p=1.96$) network generated using Barabasi-Albert algorithm with preferential attachment parameter, $m=20$. **e)** Average path length and clustering coefficient for SW network as a function of rewiring probability p . The small-world measure ranges between -1 (fully ordered network, blue) to 1 (fully random network, red), with values close to zero (white) corresponding to a perfect small-world network. The clustering coefficient and average path length for MB correspond to a small-world measure of 0.37 (vertical black line), close to 0. **f)** Degree distribution of SW, SF, and MB networks. Both MB and SF network degree distributions fit the power law distribution with exponent $\gamma=-2$. SW shows a Gaussian degree distribution. **g)** (Top) Network of interconnected Kuramoto oscillators, where each oscillator is coupled with every other oscillator through adaptive coupling (a_{ij}). (Bottom) Resource constraint implies that each oscillator is connected to individual resource reserves (battery), which define the excitability resources of the system (λ_i). The local synchrony determines the rate of energy consumption as well as the strength of local interactions.

79

80 Depending on the resource availability, our model exhibits desynchronized activity, bistability of
81 desynchronized and hyper-synchronized activity (i.e. tES) as well as steady-state hyper-synchronized activity
82 in SFNs, SWNs and the MBN. Furthermore, during the sudden transition to the synchronized state, we observe
83 a wave-like propagation of synchronization across subnetworks within the MBN, beginning with
84 cortico-thalamic subnetworks, followed by subcortical and deeper subnetworks. We also develop a novel
85 algorithm to analyze how the synchronization propagates across individual nodes (brain areas) in the MBN and
86 identify key brain areas that may be responsible for initiation, sustenance and propagation of the
87 hyper-synchronized state. Our results agree with several observations from experimental studies, suggesting
88 that a few key parameters can successfully capture the network level phenomenology of seizure dynamics.
89 Finally the model allows us to study the relationship between the hyper-synchronized state and the resource
90 consumption to recovery rate ratio. Specifically, the model predicts an optimal intermediate ratio for which the
91 likelihood of tES, i.e. epileptic attacks, is minimal. This and related predictions of our model should be directly
92 testable in experiments.

93 Results

94 An oscillator network model for transient explosive synchronization (tES) based on adaptive coupling 95 and resource constraint

96 Our model consists of N sinusoidal oscillators that form the nodes of a network. Following the Kuramoto model,
97 the interactions between connected oscillators depend on their phase difference. The interaction strength is
98 determined by the structural weight of the connection, and is further modulated by both the synchronization
99 levels of neighboring nodes and the availability of excitability resources (Fig. 1g).

100 The dynamics of the network are governed by the following equations:

$$101 \quad \dot{\theta}_i = \omega_i + \lambda_i r_i \sum_{j=1}^N A_{ij} \sin(\theta_j - \theta_i) \quad (\text{Eqn. 1})$$

102 Here, $i \in [1, N]$, θ_i and $\dot{\theta}_i$ are instantaneous phase and angular velocity of the i^{th} oscillator, and ω_i is its natural
103 frequency, uniformly distributed in $[-1, 1]$. The adjacency matrix A_{ij} encodes the network structure.

104 The interaction strengths are modulated by the local synchrony parameter,

$$105 \quad r_i = (1/k_i) \left| \sum_{j=1}^N A_{ij} e^{i\theta_j} \right|, \text{ where } k_i = \sum_{j=1}^N A_{ij} \text{ is the degree,} \quad (\text{Eqn. 2})$$

106 giving rise to adaptive coupling, whereby nodes with higher local synchrony get coupled more strongly.

107 The interactions are also modulated by the availability of resources to individual nodes, λ_i . Following the model
108 by Frolov & Hramov¹⁹, we model the time-varying nature of excitability through diffusive coupling as follows:

$$109 \quad \dot{\lambda}_i = \alpha(\lambda_o - \lambda_i) - \beta r_i \quad (\text{Eqn. 3})$$

110 where the first term represents the recovery of excitability resources at a rate α , and the second term
111 represents the local synchrony-dependent resource consumption at a rate βr_i . β is the maximal consumption
112 rate (when $r_i = 1$). The capacity of the resource reserve for each node is denoted by λ_o (size of resource bath).

113 The macroscopic behavior of the network is characterized by the global synchrony parameter,

$$114 \quad R = (1/N) \left| \sum_{i=1}^N e^{i\theta_i} \right|, \quad (\text{Eqn. 4})$$

115 which ranges from 0 (complete desynchronization) to 1 (complete synchronization).

116 A Small World Network (SWN) shows tES with adaptive coupling and resource constraint

117 We begin by investigating the properties of our model in an SWN. For this, we generate an SWN comprising
118 400 nodes while maintaining parameters such as average degree ($\langle k \rangle = 40$), average path length ($L_p = 1.97$), and
119 clustering coefficient ($C_p = 0.37$) similar to the MBN for later comparison (Fig. 1a).

120 We first characterize the resource-dependence of the network dynamics in the absence of resource dynamics
121 (Fig. 2a). Thus, in equation 1, λ_i is replaced by Λ , a fixed resource available to each node at all times. We

simulate this model with varying Λ and observe the steady-state behavior. For this, we begin with $\Lambda = 0$, adiabatically increase (decrease) Λ with increment (decrement) of $\Delta\Lambda = 0.003$, simulate the model for 1000 time steps and compute the stationary value of global synchrony (R) (see methods), going up to $\Lambda = 0.12$. For very small Λ the network exhibits normal activity, and for very high values of Λ , it goes into the hyper-synchronized state.

Interestingly for intermediate values, as Λ is slowly varied, we observe an abrupt first-order irreversible transition, with the presence of a hysteresis region – depending on the direction of change of Λ , or in other words, depending on the current state of the dynamics, the network goes into either the normal or the hyper-synchronized state (Fig. 2a).

Such existence of hysteresis has been shown to give rise to tES when resource constraint is imposed (Eqn. 3)¹⁹. When sufficient resources become available, the network transitions to the hyper-synchronized state. This transition is characterized by a sharp decrease in available resources due to increased consumption (Fig. 2d,e). Depending on the resource availability, the network spends a finite amount of time in this state before returning to the incoherent state as resources become depleted. The system replenishes its resources while in the incoherent state and transitions back to the hyper-synchronized state once sufficient resources become available.

Towards testing this hypothesized mechanism for tES, we first identify the parameter range for which the full model shows bistability, i.e. the network spends time in two (meta)stable states (Fig. 2b). We impose resource constraint at a consumption rate $\beta (= 0.002)$ and again simulate the full model for λ_o , the size of the resource bath, varying between 0.01 and 0.3 with an increment of 0.01. For each value of λ_o , we simulate the model for 1000 time steps, and observe the range of values taken by the global synchrony parameter over the simulated period. The resulting bifurcation diagram reveals that the SWN exhibits a globally incoherent state for $\lambda_o < 0.095$, where resources are too limited to allow hyper-synchronization; and a hyper-synchronized state for $\lambda_o > 0.21$. For intermediate values of λ_o the network shows a coexistence of both states, reflecting the presence of tES, as seen in the timeseries of the global synchrony parameter (Fig. 2d,e). Consistent with the proposed mechanism, the transitions to and from the hyper-synchronized state occur when the mean resource availability across all nodes is close to the corresponding critical values of Λ , as revealed in the state-space trajectory of the system (Fig. 2c).

Since the transition back to the incoherent state occurs due to resource depletion, we expect the network to spend longer time in the

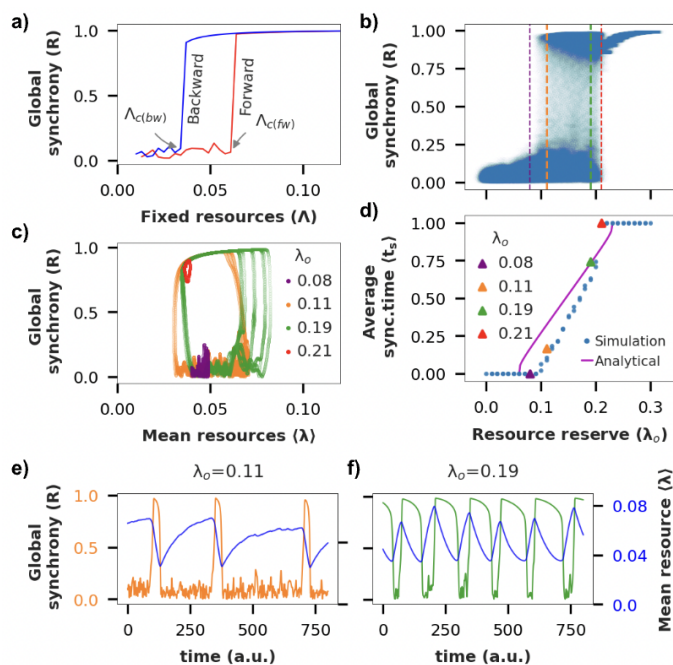


Figure 2: Resource-constrained SWN exhibits tES

a) Forward (red) and backward (blue) transition curves for an SWN with adiabatically increasing (decreasing) fixed resource level, Λ . Arrows indicate critical points corresponding to forward (or backward) transition from unordered (ordered) to ordered (unordered) state of the network. **b)** Bifurcation diagram of global synchrony (R) vs λ_o for SWN with resource constraint. **c)** $(\langle\lambda\rangle, R)$ state space trajectory of activity for different values of λ_o . **d)** Fraction of time spent in the synchronized state (average synchronized time) vs λ_o . **e, f)** Global synchrony and instantaneous mean resource level as a function of time for two different values of λ_o chosen from the bistable region in (b). Note: λ_o (fixed) is the fixed resources and $\langle\lambda\rangle$ (varying) is the instantaneous mean resources (averaged over all nodes) of the system.

hyper-synchronized state as the size of the resource bath, λ_o , increases. This prediction is supported in our simulation results (Fig. 2d) as well as with a simple analytical calculation (see supplement).

Finally we note that the phenomenon of ES or tES is not observed with SWN when correlation feature-based connectivity, such as FDC, is used¹⁹.

The mesoscale mouse brain network (MBN) shows partial tES with adaptive coupling

Next we use our model to study tES in a real biological neural network, using the mouse brain mesoscale connectivity data from the Allen Brain Atlas. The mesoscale atlas is constructed by injecting viral vectors to trace axonal projections across pairs of brain regions in mice²¹. The dataset consists of detailed and accurate connectivity information across 426 brain areas spanning both hemispheres (see Methods) in healthy mice. The resulting network (Fig. 1d) comprises 11,000 directed edges, with weights rescaled between 0 and 1.

We repeat the analyses from SWN on MBN with an added nuance: while we assumed the SWNs to be binary undirected networks, the dataset we use allows us to define the MBN as a weighted directed network. To account for this, we use a modified version of equations 1 and 2 (see supplement). We analyze all three variants of the MBN – binary-undirected, binary-directed, and weighted-directed. The results presented below refer to the most complete weighted-directed variant unless mentioned otherwise, while the results for the other two variants are qualitatively similar (Fig. S4).

We again begin by characterizing the system with fixed resource availability (see Methods for details). Surprisingly, unlike the SWN which showed hysteresis, the MBN shows bistability for intermediate values of fixed resources ($\Lambda \in [2.58, 2.65]$) (Fig. 3a). Even binary-undirected and binary-directed versions of MBN, show hysteresis but not bistability for fixed resources (Fig. S4a, S4b). It is important to note that when examining a network with fixed resources, the hysteresis region indicates the potential for tES, but does not guarantee it. On the other hand, the presence of the bistability region directly confirms the existence of tES for the weighted-directed MBN even without the need for resource constraint. We further confirm the existence of tES with simulations of the full model that includes resource constraint (Fig. 3b-d, S3). Note that with the FDC model with or without resource constraints we are unable to induce tES in the MBN (Fig. S4f, S4g).

Our analysis of the MBN recapitulates the observations from SWN, including the increasing time spent in the synchronized state with increasing size of resource bath (Fig. 3b inset). An interesting deviation is that the synchronized state is only partially synchronized, as reflected in the global synchrony parameter only reaching up to 0.6 instead of 1 (Fig. 3a-d). This happens because certain subnetworks within the MBN never participate in the synchronization. We thus define actively participating nodes as those with a local synchrony greater than the threshold value of 0.7 during the partially synchronized state. We then compare the state space trajectory obtained by averaging the available resources over all nodes versus averaging only over the actively participating nodes (Fig. S2). The state space trajectory shifts to the right in the former case,

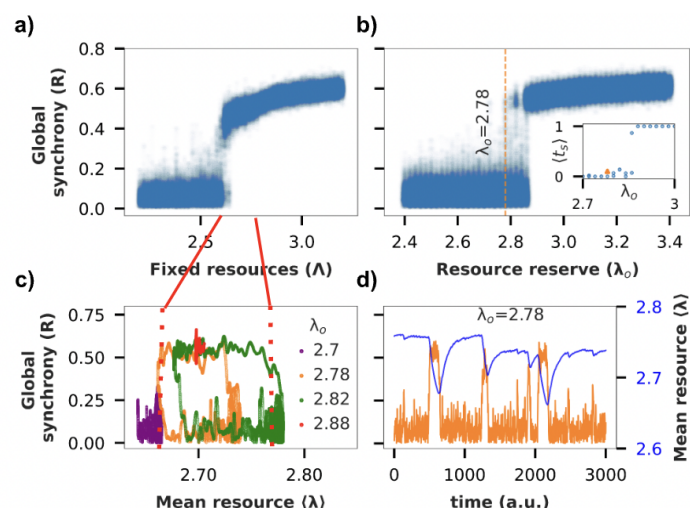


Figure 3: Mesoscale MBN with excitability resource constraint exhibits tES

a) Bifurcation diagram of global synchrony (R) vs Λ for the weighted MB network. **b)** Bifurcation diagram of global order (R) vs λ_o for the resource constrained model. (Inset) Fraction of time spent in synchronized state vs λ_o . **c)** $(\langle \Lambda \rangle, R)$ state space trajectory of activity for different values of λ_o . **d)** Time series of global synchrony vs instantaneous resources.

suggesting that inactive nodes are pushing the average available resources ($\langle \lambda \rangle$) to higher value. We thus conclude that only the nodes that actively participate in the synchronization cluster increase their energy consumption during tES.

Another deviation from SWNs is that the average resource level (even after restricting to participating nodes) at the time of transitions is observed to be higher than the corresponding resource level in the fixed resource model (Fig. 3a,c). One hypothesis is that even within the synchronized cluster, there may be a core subcluster that drives tES, for which the average energies at transition may be lower, but the peripheral nodes in the synchronized cluster, with higher energy availability, push the apparent average transition energy levels higher. This, however, does not seem to be the case. We conclude that the higher complexity of biological networks, perhaps due to their modular, hierarchical and heterogeneous nature compared to the SWN, makes the relationship between the fixed resource and resource constrained dynamics less predictable.

In the following sections we investigate the dynamics of propagation of synchronization in the MBN.

ES propagates as a wave from cortico-thalamic to subcortical subnetworks within the MBN

We group the 426 nodes in MBN into distinct communities purely based on the network structure, using the Louvain algorithm (see Methods)²². We hypothesize that such structure-based partitioning of the nodes will group together nodes that are highly likely to form a synchronization cluster. The process naturally partitions the MBN into 8 communities which can be clubbed into three broad classes: cortico-thalamic (4 communities), subcortical (3 communities) and hindbrain (Fig. 4a).

We then generate a set of 52 transitions from the incoherent to the hyper-synchronized state by running 4 long simulations, with fixed $\lambda_0 = 2.87$, but with different initial conditions (see Methods). Each transition is characterized by the presence of an 'onset index', a point where nearly complete desynchronization occurs just before the abrupt transition is about to begin (Fig. 4b, inset), subsequent to which synchronization rapidly increases. To study the spatial propagation of synchronization within the short temporal window in which it occurs, we analyze the transient dynamics over a 50 time unit window following the onset index.

We first study the dynamics of synchronization during the transient window within each community, by computing the intra-modular synchrony (a measure of phase alignment across nodes within

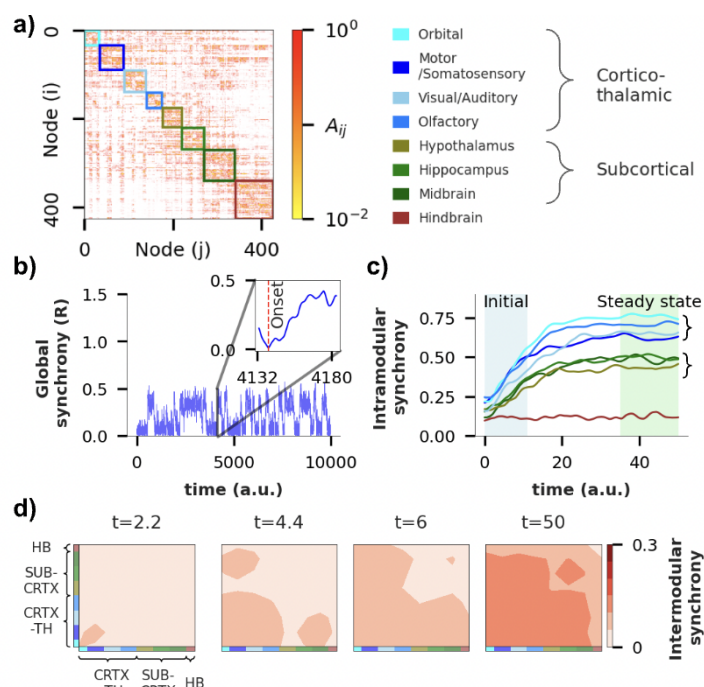


Figure 4: ES propagates as a wave across MBN communities

a) Adjacency matrix of MBN where coloured boxes group the 426 nodes into 8 distinct communities obtained using the Louvian algorithm with a resolution parameter of 1. Communities are named based on underlying circuitry (see Supplementary figure 5) and can be further grouped into broader categories: cortico-thalamic (blue) and subcortical (green). Modularity score (Q) of the obtained community partition is 0.53. **b)** The global synchrony parameter reflects several tES events in a weighted MBN for $\lambda_0 = 2.87$. (Inset) activity for one of the transients (out of 52 total) starting from the 'onset index' (red vertical line), characterized by the point where complete desynchronization occurs just before the abrupt transition. **c)** **Intramodular synchrony** (synchronization level within each community averaged over all 52 transients) during the transition shown in (b). Colors represent communities from (a). **d)** Contour map of **intermodular synchrony** for 4 different time points, spanning from a time close to 'onset index' ($t=2.2$) to the time post abrupt transition ($t=50$) reveals a wave propagating across the network.

the community, see Methods) averaged over all 52 transients. Based on the temporal evolution of the intramodular synchrony, we can group the 8 communities into three distinct cohorts that overlap perfectly with the structural classes defined earlier: cortico-thalamic, subcortical, and hindbrain (Fig. 4c). The steady-state intra-modular synchrony is significantly higher for the cortico-thalamic communities, followed by subcortical, and finally hindbrain, which shows no internal synchronization ($p < 10^{-4}$ for all the three pairs).

At the start of the transient process, the orbital, olfactory and sensorimotor areas exhibit significantly higher intra-modular synchrony than the rest of the communities ($p < 0.05$ for each pair, Fig. S8), and also show a steeper rate of increase (Fig. S8), indicating their potential role in initiating and driving the abrupt transition. As the transient progresses, orbital and olfactory areas consistently maintain a significantly higher level of synchronization compared to the rest ($p < 0.05$, Fig. S8). These results suggest that, while the onset sites of tES can be the orbital, olfactory, or sensorimotor areas, it is likely that the orbital and olfactory areas play a dominant role in driving the transition throughout the entire duration of the transient process. We note that, while intramodular synchrony in the visual area does not seem to significantly differ from the orbital area (Fig. S8), it shows much higher trial to trial variation in terms of its participation. This reinforces previous observations in the literature that the visual area is not critical for the propagation of synchronization²³.

The dynamics of synchronization propagation can be understood by analyzing the inter-modular synchrony between community pairs (see Methods). Consistent with what we found earlier, ES initiates in the orbital and sensorimotor areas (Fig. 4d, $t = 2.2$), and then spreads across all cortical regions (Fig. 4d, $t = 4.4$). Notably, the hippocampal / midbrain areas synchronize with cortical areas before synchronizing among themselves (Fig. 4d, $t = 4.4, 6, 50$), indicating that the cortical areas are driving their synchronization. At steady state ($t = 50$), all cortical, thalamic, and subcortical regions achieve synchrony, while hindbrain exhibits minimal participation throughout. Overall, these findings suggest a hierarchical synchronization process, with cortical areas potentially driving synchronization among subcortical regions.

Propagation of ES across individual nodes in the MBN reveals critical nodes that drive ES

Going beyond the community level, below we assess synchronization propagation at a single node level. Assessing the synchronization between individual nodes typically involves computing the correlation of activity of the pair over short time windows^{24,25}. However, given the extremely short-lived transition window, this technique cannot provide sufficient temporal resolution for studying abrupt transitions. We therefore came up with a novel algorithm that we call the Synchronization Cluster Tracking Algorithm (SCTA) (see methods) for this analysis. The SCTA employs a two-step procedure for quantifying the participation of individual nodes in the synchronization process: (1) generating synchronization clusters by starting from a seed node and expanding the cluster till the local synchrony drops below a fixed threshold; and (2) tracking the synchronization clusters progressively through time to get a 'cluster lineage' for each node (see Methods). We apply SCTA to all 52 transients with a local synchrony threshold of 0.5 for the subsequent analysis, although the choice of threshold does not change the results qualitatively (Fig. S5).

The transition typically begins with multiple small synchronization clusters (cluster size < 10) during the early phase (Fig. 5a, $t \approx 17$). As the transition progresses, we observe the emergence of a 'main synchronization cluster' that quickly comes to dominate in size (Fig. 5a) throughout the rest of the transition. The size of the main cluster varies as the small peripheral clusters or individual nodes continue to join or leave it. This indicates that while the specific onset sites may vary across different trials initially, once the abrupt transition begins, it rapidly spreads from that initial onset site to encompass a broad set of core nodes that hold it together.

To test the 'core' nodes hypothesis, we quantify the time spent by individual nodes in the main synchronization cluster across the 52 transients. We find that although a majority of the nodes exhibit participation in the main

synchronization cluster, certain nodes consistently spend a significant amount of time in the main cluster (median time spent > 35, std. dev. < 10, Fig. 5b). This core spans across multiple brain areas including the cortex (19 nodes), hippocampus (6), striatum (9), thalamus (10) and the midbrain (3). In contrast, nodes with high variability likely represent peripheral nodes that frequently attach and detach from the main cluster, contributing to the observed variation in cluster size.

This analysis allows us to hypothesize the existence of driver nodes for hyper-synchronization, as nodes with consistent, high participation, and a high out-degree. By spending longer times in the main synchronization cluster, and influencing several downstream nodes they are likely to play a key role in the propagation of synchronization (Fig. 5c). Numerous other nodes with lower out degrees also consistently spend more time in the main cluster, indicating their higher susceptibility to the influence of the drivers, rather than themselves influencing other nodes. These driver areas include the Perirhinal (PERI), Entorhinal (ENTI), Orbital (ORBI), Reticular Nucleus (RE), Basolateral Amygdala (BLA), Piriform (PIR) and Agranular insular area (Ai). Notably, a majority of these "driver nodes" are located in cortical areas. The hindbrain spends the least time in the main cluster, consistent with our earlier findings.

An intermediate resource recovery-to-consumption ratio is optimal

Since we model resource dynamics explicitly, our model allows us to investigate the impact of resource dynamics on the propensity of tES for the network. In particular, we study the impact of the resource recovery-to-consumption rate ratio (α/β) by fixing the recovery rate ($\alpha = 0.01$) and varying the consumption coefficient ($\beta \in \{0.01, 0.005, 0.002, 0.001, 0.0005, 0.00025, 0.0002\}$). For this set of parameters, we identify the range of resource bath size (λ_0) that support tES. We find that as the recovery-to-consumption rate ratio increases, both SWN and MBN exhibit a shift in the range boundaries to lower values, indicating a higher propensity for tES at low resource levels (Fig. 6a,b). The exponential decrease in range boundaries with an increase in the ratio suggests that even a slight change in the recovery-to-consumption ratio can significantly alter the network's propensity to generate tES.

In contrast, as the recovery-to-consumption rate ratio increases, the width of the bistability region decreases. Moreover, within the bistable region also, the duration of time spent in the synchronized state decreases, resulting in a decreased probability of tES occurrence (Fig. 6c).

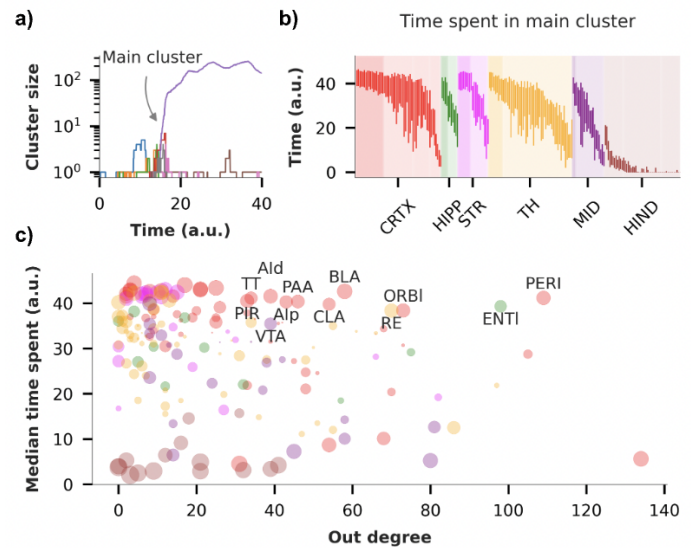


Figure 5: Participation of individual nodes in the main synchronization cluster during the transition

a) Synchronization clusters for the transient shown in Fig. 4b obtained using Synchronization Cluster Tracking Algorithm (SCTA) with synchronization threshold of 0.5 (Supplementary material). The figure illustrates one main synchronization cluster (purple, ~200 nodes) along with several smaller clusters (~2-20 nodes). **b)** Box plot of the time spent by each node in the main synchronization cluster for 52 different transients (only left hemisphere nodes are shown for clarity). Nodes are color coded as per the major regions defined in Fig. 1c. Dark shaded area in each region shows node with median time spent > 35, and variance in time spent < 49 ($\sigma < 7$). **c)** Median time spent in the main synchronization cluster vs out degree of nodes in the left hemisphere (limited to 213 nodes). The size of the scatter points is inversely proportional to the variance in time spent across 52 transients, with larger circles indicating low variance. Labeled points indicate nodes with out-degree > 30, median time spent > 35, and variance in time spent < 49.

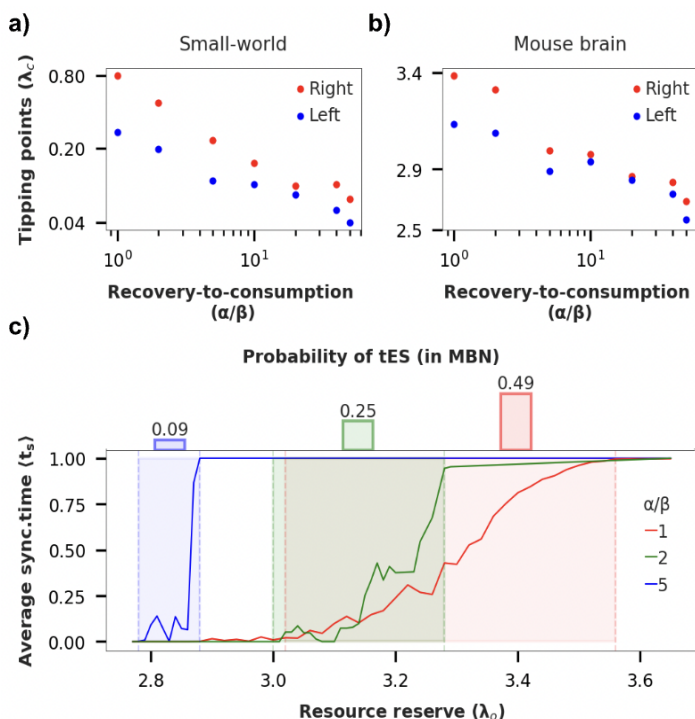


Figure 6: Effect of resource consumption coefficient (β) on network dynamics

a, b) Critical value of λ_o corresponding to left (blue) and right (red) tipping points of the bistability region as function of recovery-to-consumption ratio (or metabolism-to-uptake ratio). Note: Both x and y-axis are on log scale. **c)** (bottom) Fraction of time spent in synchronized state, (average synchronized time) $\langle t_s \rangle$ vs λ_o (bistable region shaded). (top) Probability of tES occurrence as function of recovery-to-consumption rate ratio (α/β) (estimated by measuring area under curve in shaded region normalized by area of shaded region).

Together, these results suggest an optimal intermediate ratio for a healthy brain as follows (Fig. 6d): Assume that the brain always operates at a resource bath size such that it is near the bistable region (criticality hypothesis^{17,26}). Moreover, the resource bath size also undergoes fluctuations. In this scenario, a very low ratio would mean a high probability of tES, i.e. a high likelihood of seizures. If the ratio is very high, the width of the bistable region is so small that fluctuations in the resource bath size push the brain into the monostable hypersynchronized state, again increasing the likelihood of seizures. But an intermediate value of the ratio ensures a balance between these two extremes, and should be observable in a healthy brain.

Discussion

We first show in an idealized SWN (and other topologies such as SFN) how adaptive coupling can give rise to resource level-dependent hysteresis. Upon the addition of resource dynamics, this gives rise to tES for intermediate sizes of the resource bath. Recent research comparing diffusive and adaptive coupling, common modeling choices in networks of neural masses, has demonstrated a higher likelihood of networks with adaptive coupling to generate seizures²⁰. Our findings reinforce this preference for adaptive coupling in exhibiting a higher tendency for

Our results hold well qualitatively when we apply the same model to a real biological neural network – the mesoscale mouse brain network from the Allen Brain Atlas (Fig. 3). Although the structural network comes from healthy, rather than epileptic mice, our results demonstrate the ability of the model to generate seizure-like dynamics in a biologically realistic network. The framework can be used to further study how perturbations to this network can increase their susceptibility to seizures, thus understanding the specific potential structural elements in diseased mice (or humans) that lead to epilepsy. The choice of a mouse brain as the model system is made because of the greater precision and completeness with which the anatomical connectivity can be measured, compared to non-invasive methods employed in humans.

At the same time, for the MBN we observe some very interesting deviations compared to SWNs. The MBN reaches only a partially synchronized state, with specifically the hindbrain subnetwork never participating in the synchronization (Fig. 3). Even within the synchronized cluster, we hypothesize the presence of a core that becomes fully synchronized, and drives the tES event, and a periphery that does not necessarily reach full synchronization. The energy levels of the nodes at the time of transition may provide a means to identify the core and the periphery. Moreover, the constitution of this core likely depends on the size of the resource bath, so that for different bath sizes, we observe different average transition energies (Fig. 3c). We speculate that

this added complexity is a result of the weighted, hierarchical and modular network structure in real brains compared to our idealized SWN. These hypotheses and speculations are areas for further study to understand how the network structure affects its susceptibility to tES.

We then study the dynamics of synchronization propagation across the network at the level of communities (aka subnetworks) and individual nodes. A salient feature we observe is that preceding each abrupt transition, there is a point of near-complete desynchronization across the network (Fig. 4b-inset). This is accompanied by the formation of several small clusters which later merge into the main synchronization cluster. These phenomena are consistent with results obtained through mean field analyses^{14,25}, as well as experimental observations at micro- and macroscopic levels^{27–30}.

At the intra-community level, we find that the cortico-thalamic networks (particularly the orbital, olfactory and sensorimotor areas) exhibit a higher starting synchrony, faster increase of synchrony and a higher steady-state synchrony during the transitions, compared to subcortical communities (Fig. 4c). This suggests their role in initiating and propagating the hyper-synchronized state, consistent with extensive observations and predictions in literature^{31–36}. Additionally, we find certain cortical networks (orbital, sensorimotor) to be more critical for synchronization propagation than others (visual)²³.

Quantification of inter-modular synchronization reveals that the synchronization expands in a hierarchical manner, as a propagating wave from the cortical to subcortical regions (Fig. 4d), so that the subcortical areas synchronize with cortical areas before they synchronize among themselves. Although whole-brain recordings during generalized epilepsy are lacking, this would be an interesting hypothesis to test in model organisms with invasive electrophysiology.

We develop a novel algorithm to track the synchronization cluster lineages for individual nodes, which reveals the existence of a single large synchronization cluster during the transition, with several small clusters that dynamically join or leave it. Based on the consistency and time spent by the nodes in the main cluster, and their out degrees, we find a set of ‘core’ nodes that hold the cluster together, irrespective of the initiating site. This driver set includes Perirhinal, Entorhinal, Orbital, Reticular Nucleus, Basolateral Amygdala, Piriform and Agranular insular areas. These predictions are supported by several experimental findings^{37,38}: for instance, the entorhinal, perirhinal, and piriform cortex form a highly interconnected network with other limbic structures and have been shown to possess characteristics that make them susceptible to the initiation and spread of epileptic seizures³⁹.

According to theoretical analysis¹⁴ and our cluster tracking results, abrupt transitions during tES are preceded by the formation of numerous small synchronization clusters. This is consistently preceded by almost complete desynchronization. The more of these clusters, the more abrupt the transition¹⁴. A similar phenomenon of synchronization cluster formation and interictal/preictal desynchronization is observed before critical transitions during seizures^{28,29,41}. Experimental evidence shows that these individual clusters exhibit high-frequency oscillations (HFOs) of 80-500 Hz⁴¹. These observations suggest that the preictal/interictal dynamics of HFO may vary depending on the seizure class that exhibits preictal desynchronization. Testing this hypothesis is intriguing, as it could emphasize the importance of considering seizure type when using HFO as a biomarker⁴⁰.

Lastly, our mechanistic model highlights the importance of an intermediate resource recovery-to-consumption ratio, effectively balancing the heightened tES likelihood and the occurrence of monostable hypersynchronous activity. This implies an optimal recovery-to-consumption range where seizures are infrequent⁴², and a constant hypersynchronous state is improbable. Deviations from this range may trigger abnormal brain states, suggesting a testable hypothesis for the susceptibility to epileptic attacks in relation to ATP demand and oxygen consumption rates observed during ictal and interictal epileptiform activity^{43,44}.

427 To summarize, our mesoscale network model for generalized epilepsy applied to a real biological brain network
428 makes several predictions that are consistent with experimental data and more biologically realistic and
429 complex models. The simplicity, coupled with the generality, of the model holds significant value for two key
430 reasons: first, its simplicity allows for the simulation of large-scale brain networks without significant concerns
431 about computational load; and second, it potentially enables the study of seizure dynamics in a wide range of
432 whole-brain networks, and could have applicability from a translational perspective. By identifying the
433 propagation pattern during seizures, we can potentially identify strategies to halt the propagation. Therefore,
434 the model and techniques developed here can be applied to connectome data from actual epileptic brains, with
435 the hope of identifying the seizure onset site and its progression.

436 Methods

437 Simulations

438 To evaluate the dynamics of the model with different network structures (small-world, scale-free, mouse brain),
 439 we perform two types of simulations: adiabatic progression and bifurcation diagram construction. In the
 440 adiabatic progression, we systematically increase or decrease the fixed resource Λ to observe the global order
 441 of the conventional adaptive coupling model with fixed resources. This allows us to determine the hysteresis
 442 region of the system. For the bifurcation diagram construction, we increase the resource bath size parameter
 443 λ_o and measure the global order at each time point. For all simulations, we use $\alpha = 0.01$, $\beta = 0.002$ (unless
 444 otherwise specified) and the initial phases θ_i are distributed uniformly in the range $[0, 2\pi)$. Equations are
 445 simulated using the Euler method with a step size of 0.05.

446 To construct hysteresis (bifurcation) diagram in MBN, unlike SWN, we run simulations for a duration of 2000
 447 time units for each value of Λ / λ_o through adiabatic progression with $\Delta\Lambda = 0.02 / \Delta\lambda_o = 0.02$.

448 To study the progression of ES in a weighted MBN, we conduct four separate runs with a fixed value of
 449 $\lambda_o = 2.87$, each using distinct initial conditions for (phase) θ and (frequency) ω . The simulations spanned a
 450 duration of 20000 time units. From these simulations, we extract a total of 52 transients by selecting segments
 451 of length 50-time units, starting from the “onset index” just before the abrupt transition.

452 Data Analysis

453 Intramodular synchrony:

454 At any particular time unit during the simulation, to assess synchrony level among nodes belonging to one
 455 community (obtained from community detection algorithm), intramodular (within community) synchrony, for
 456 each community, is computed as the average coherence of phase alignments of all the nodes:

$$457 \quad IMS_c = 1/N_c \left| \sum_{i=1}^{N_c} e^{i\theta_i} \right|$$

458 where, IMS_c is intra-modular synchrony is for the c^{th} community and N_c is the number of nodes. The average
 459 intra-modular synchrony ($\overline{IMS_c}$) is computed by averaging the synchronization level (IMS_c) within each
 460 community across 52 transients:

$$461 \quad \overline{IMS_c} = \sum_{tr=1}^{52} \left(1/N_c \left| \sum_{i=1}^{N_c} e^{i\theta_i^{tr}} \right| \right)$$

462 This calculation is performed for each time point within a 50-time unit window to capture the temporal evolution
 463 of intra-modular synchrony during the period of abrupt transition.

464 Intermodular synchrony:

465 To compute coherence between two distinct communities, intermodular synchrony is computed as the average
 466 absolute value of pairwise sum of phase alignment between nodes belonging to different communities:

$$IMS_{c_1 c_2} = 1/(N_{c_1} N_{c_2}) \left| \sum_{i=1}^{N_{c_1}} \sum_{j=1}^{N_{c_2}} 0.5 * (e^{i\theta_i} + e^{i\theta_j}) \right|$$

where, N_{c_1} and N_{c_2} is number of nodes in community c_1 and c_2 . To get temporal evolution of inter-modular synchrony, the average value across 52 transients is computed using a similar methodology as employed for intramodular synchrony analysis.

Synchronization cluster tracking algorithm:

The Synchronization cluster tracking algorithm (SCTA) performs two major tasks: i) finds the synchronization clusters at each time unit (Fig. SM1), ii) tracks the temporal evolution of identified clusters across different time units (Fig. SM2).

The SCTA aims to expand synchronization clusters within the network based on a given synchronization threshold. It follows three key steps:

1. Expansion around Central Nodes: The algorithm begins by expanding the synchronization clusters around the central nodes, which are selected from the previous time step. These central nodes act as trackers for the clusters across different time steps. Nodes with local synchrony exceeding a predetermined threshold become part of the cluster, which terminates with nodes that fall below the threshold (Fig. SM1).
2. Expansion for Unassigned Nodes: Next, the algorithm expands the synchronization clusters for any nodes that have not yet been assigned to a cluster. This step ensures that all nodes are considered and included in appropriate clusters based on the synchronization threshold (Fig. SM2).
3. Update Central Node List: Finally, once all nodes have been traversed or become part of some cluster, the algorithm updates the list of central nodes for each cluster. Central nodes are the top 5 nodes in each cluster with highest local synchrony. These central nodes are important reference points for the clusters, preserving their cluster membership over time, and acting as seed nodes for the expansion of clusters in the next time step (Fig. SM2).

By following these steps iteratively, the algorithm progressively identifies, expands, and tracks synchronization clusters within the network.

Time spent in main synchronization cluster:

By executing the SCTA over a 50-time unit window for a specific transient, we obtain the cluster sizes as a function of time. The largest cluster is defined as the main synchronization cluster, and we measure the time spent by each node as part of the main cluster within the 50 time step window.

496 References

- 497 1. Da Silva, F. L. *et al.* Epilepsies as Dynamical Diseases of Brain Systems: Basic Models of the Transition
498 Between Normal and Epileptic Activity. *Epilepsia* **44**, 72–83 (2003).
- 499 2. Sarmast, S. T., Abdullahi, A. M. & Jahan, N. Current Classification of Seizures and Epilepsies: Scope,
500 Limitations and Recommendations for Future Action. *Cureus* **12**, e10549.
- 501 3. Richardson, M. P. Large scale brain models of epilepsy: dynamics meets connectomics. *J. Neurol.*
502 *Neurosurg. Psychiatry* **83**, 1238–1248 (2012).
- 503 4. Bromfield, E. B., Cavazos, J. E. & Sirven, J. I. *Basic Mechanisms Underlying Seizures and Epilepsy. An*
504 *Introduction to Epilepsy [Internet]* (American Epilepsy Society, 2006).
- 505 5. Gleichgerricht, E., Kocher, M. & Bonilha, L. Connectomics and graph theory analyses: Novel insights into
506 network abnormalities in epilepsy. *Epilepsia* **56**, 1660–1668 (2015).
- 507 6. Terry, J. R., Benjamin, O. & Richardson, M. P. Seizure generation: The role of nodes and networks.
508 *Epilepsia* **53**, e166–e169 (2012).
- 509 7. Berg, A. T. *et al.* Revised terminology and concepts for organization of seizures and epilepsies: report of
510 the ILAE Commission on Classification and Terminology, 2005–2009. *Epilepsia* **51**, 676–685 (2010).
- 511 8. Chowdhury, F. A. *et al.* Revealing a Brain Network Endophenotype in Families with Idiopathic Generalised
512 Epilepsy. *PLOS ONE* **9**, e110136 (2014).
- 513 9. Petkov, G., Goodfellow, M., Richardson, M. P. & Terry, J. R. A Critical Role for Network Structure in Seizure
514 Onset: A Computational Modeling Approach. *Front. Neurol.* **5**, (2014).
- 515 10. Jirsa, V. K., Stacey, W. C., Quilichini, P. P., Ivanov, A. I. & Bernard, C. On the nature of seizure dynamics.
516 *Brain* **137**, 2210–2230 (2014).
- 517 11. Gerster, M. *et al.* FitzHugh-Nagumo oscillators on complex networks mimic epileptic-seizure-related
518 synchronization phenomena. *Chaos Interdiscip. J. Nonlinear Sci.* **30**, 123130 (2020).
- 519 12. Gomez-Gardenes, J., Gomez, S., Arenas, A. & Moreno, Y. Explosive Synchronization Transitions in
520 Scale-free Networks. *Phys. Rev. Lett.* **106**, 128701 (2011).
- 521 13. Leyva, I. *et al.* Explosive synchronization in weighted complex networks. *Phys. Rev. E* **88**, 042808 (2013).
- 522 14. Zhang, X., Boccaletti, S., Guan, S. & Liu, Z. Explosive synchronization in adaptive and multilayer networks.
523 *Phys. Rev. Lett.* **114**, 038701 (2015).
- 524 15. Kramer, M. A. & Cash, S. S. Epilepsy as a disorder of cortical network organization. *Neurosci. Rev. J.*
525 *Bringing Neurobiol. Neurol. Psychiatry* **18**, 360–372 (2012).
- 526 16. McSharry, P. E., Smith, L. A. & Tarassenko, L. Prediction of epileptic seizures: are nonlinear methods
527 relevant? *Nat. Med.* **9**, 241–242 (2003).
- 528 17. Kim, M., Harris, R. E., DaSilva, A. F. & Lee, U. Explosive Synchronization-Based Brain Modulation
529 Reduces Hypersensitivity in the Brain Network: A Computational Model Study. *Front. Comput. Neurosci.*
530 **16**, (2022).
- 531 18. Wang, Z., Tian, C., Dhamala, M. & Liu, Z. A small change in neuronal network topology can induce
532 explosive synchronization transition and activity propagation in the entire network. *Sci. Rep.* **7**, 561 (2017).
- 533 19. Frolov, N. & Hramov, A. Extreme synchronization events in a Kuramoto model: The interplay between
534 resource constraints and explosive transitions. *Chaos Interdiscip. J. Nonlinear Sci.* **31**, 063103 (2021).
- 535 20. Lopes, M. A., Hamandi, K., Zhang, J. & Creaser, J. L. The role of additive and diffusive coupling on the
536 dynamics of neural populations. *Sci. Rep.* **13**, 4115 (2023).
- 537 21. Oh, S. W. *et al.* A mesoscale connectome of the mouse brain. *Nature* **508**, 207–214 (2014).
- 538 22. Blondel, V. D., Guillaume, J.-L., Lambiotte, R. & Lefebvre, E. Fast unfolding of communities in large
539 networks. *J. Stat. Mech. Theory Exp.* **2008**, P10008 (2008).
- 540 23. Nersesyan, H., Hyder, F., Rothman, D. L. & Blumenfeld, H. Dynamic fMRI and EEG Recordings during
541 Spike-Wave Seizures and Generalized Tonic-Clonic Seizures in WAG/Rij Rats. *J. Cereb. Blood Flow*
542 *Metab.* **24**, 589–599 (2004).
- 543 24. Schmidt, R., LaFleur, K. J. R., de Reus, M. A., van den Berg, L. H. & van den Heuvel, M. P. Kuramoto
544 model simulation of neural hubs and dynamic synchrony in the human cerebral connectome. *BMC*
545 *Neurosci.* **16**, 54 (2015).
- 546 25. Zhang, X., Zou, Y., Boccaletti, S. & Liu, Z. Explosive synchronization as a process of explosive percolation
547 in dynamical phase space. *Sci. Rep.* **4**, 5200 (2014).
- 548 26. Beggs, J. M. Addressing skepticism of the critical brain hypothesis. *Front. Comput. Neurosci.* **16**, (2022).
- 549 27. Aarabi, A., Wallois, F. & Grebe, R. Does spatiotemporal synchronization of EEG change prior to absence

- 550 seizures? *Brain Res.* **1188**, 207–221 (2008).
- 551 28. Jiruska, P. *et al.* Synchronization and desynchronization in epilepsy: controversies and hypotheses. *J.*
552 *Physiol.* **591**, 787–797 (2013).
- 553 29. Mormann, F. *et al.* Epileptic seizures are preceded by a decrease in synchronization. *Epilepsy Res.* **53**,
554 173–185 (2003).
- 555 30. Wendling, F., Bartolomei, F., Bellanger, J.-J., Bourien, J. & Chauvel, P. Epileptic fast intracerebral EEG
556 activity: evidence for spatial decorrelation at seizure onset. *Brain J. Neurol.* **126**, 1449–1459 (2003).
- 557 31. Meeren, H. K. M., Pijn, J. P. M., Van Luijckelaar, E. L. J. M., Coenen, A. M. L. & Lopes da Silva, F. H. Cortical
558 focus drives widespread corticothalamic networks during spontaneous absence seizures in rats. *J.*
559 *Neurosci. Off. J. Soc. Neurosci.* **22**, 1480–1495 (2002).
- 560 32. Miao, A. *et al.* Dynamic magnetic source imaging of absence seizure initialization and propagation: A
561 magnetoencephalography study. *Epilepsy Res.* **108**, 468–480 (2014).
- 562 33. Szaflarski, J. P. *et al.* Cortical and subcortical contributions to absence seizure onset examined with
563 EEG/fMRI. *Epilepsy Behav. EB* **18**, 404–413 (2010).
- 564 34. Holmes, M. D., Brown, M. & Tucker, D. M. Are “Generalized” Seizures Truly Generalized? Evidence of
565 Localized Mesial Frontal and Frontopolar Discharges in Absence. *Epilepsia* **45**, 1568–1579 (2004).
- 566 35. Meeren, H., van Luijckelaar, G., Lopes da Silva, F. & Coenen, A. Evolving Concepts on the Pathophysiology
567 of Absence Seizures: The Cortical Focus Theory. *Arch. Neurol.* **62**, 371–376 (2005).
- 568 36. Zhong, L. *et al.* Temporal and spatial dynamic propagation of electroencephalogram by combining power
569 spectral and synchronization in childhood absence epilepsy. *Front. Neuroinformatics* **16**, 962466 (2022).
- 570 37. Chen, C. *et al.* Olfactory Auras in Patients with Temporal Lobe Epilepsy. *Epilepsia* **44**, 257–260 (2003).
- 571 38. Hamasaki, T., Otsubo, H., Uchikawa, H., Yamada, K. & Kuratsu, J. Olfactory auras caused by a very focal
572 isolated epileptic network in the amygdala. *Epilepsy Behav. Case Rep.* **2**, 142–144 (2014).
- 573 39. Vismer, M. S., Forcelli, P. A., Skopin, M. D., Gale, K. & Koubeissi, M. Z. The piriform, perirhinal, and
574 entorhinal cortex in seizure generation. *Front. Neural Circuits* **9**, 27 (2015).
- 575 40. Saggio, M. L. *et al.* A taxonomy of seizure dynamotypes. *eLife* **9**, e55632 (2020).
- 576 41. Jiruska, P. *et al.* High-Frequency Network Activity, Global Increase in Neuronal Activity, and Synchrony
577 Expansion Precede Epileptic Seizures In Vitro. *J. Neurosci.* **30**, 5690–5701 (2010).
- 578 42. Protachevich, P. R. *et al.* Bistable Firing Pattern in a Neural Network Model. *Front. Comput. Neurosci.* **13**,
579 19 (2019).
- 580 43. Schoknecht, K. *et al.* Event-Associated Oxygen Consumption Rate Increases ca. Five-Fold When Interictal
581 Activity Transforms into Seizure-Like Events In Vitro. *Int. J. Mol. Sci.* **18**, 1925 (2017).
- 582 44. Muddapu, V. R., Dharshini, S. A. P., Chakravarthy, V. S. & Gromiha, M. M. Neurodegenerative Diseases –
583 Is Metabolic Deficiency the Root Cause? *Front. Neurosci.* **14**, (2020).

584 Acknowledgements

585 AKR was supported by a research fellowship from IIT-Delhi. SRG was supported by the Young Faculty
586 Incentive Fellowship from IIT-Delhi. We are also grateful to Dr. Tapan Kumar Gandhi from IIT-Delhi and Dr.
587 Srinivasa Chakravarthy from IIT-Madras for helpful discussions on the topic.

588 Author contributions

589 AKR and SRG conceived the study, designed the model and computational framework, analyzed the data, and
590 wrote the manuscript. AKR carried out the implementation. SRG conceived the idea for the novel algorithm,
591 and in consultation with SRG, AKR further developed and refined the algorithm.

592 Code availability

593 The code and parameters that have provided the results presented here are available at GitHub
594 https://github.com/csndi-iitd/IES_mesoscale_connectivity_model.git